

1 **Persistence of melt-bearing Archean lower crust for >200 million**
2 **years – an example from the Lewisian Complex, NW Scotland**

3

4 Richard J. M. Taylor¹, Tim E. Johnson^{2,3}, Chris Clark², Richard J. Harrison¹.

5

6 ¹ *Department of Earth Sciences, University of Cambridge, Cambridge CB2 3EQ, UK*

7 ² *School of Earth and Planetary Sciences, Curtin University, Perth WA 6845, Australia*

8 ³ *State Key Laboratory of Geological Processes and Mineral Resources, China University of Geosciences, Wuhan,*

9 *Hubei Province, 430074, China.*

10

11

Supplemental Information

Table DR1. U–Pb and trace element analyses of zircon

2020059_Table DR1.xlsx

12 1. METHODS

13 1.1 Laser ablation inductively coupled plasma mass spectrometry (LA-ICP-MS)

14 Heavy mineral concentrates were separated at the University of Cambridge using a jaw crusher
15 followed by traditional magnetic and heavy liquid separation. Zircon grains were then hand-
16 picked and mounted in 25 mm epoxy discs for further analysis.

17 Collection of LA-ICP-MS data was performed at the GeoHistory Facility at the John de Laeter
18 Centre, Curtin University, Perth, Australia. Individual zircon grains were ablated using an ASI
19 RESOLUTION M-50A-LR, incorporating a Compex 193nm Ar-F excimer laser attached in Split
20 Stream (LASS) mode (Kylander-Clark et al., 2013) to a Nu Instruments Nu-Plasma2 HR multi-
21 collector (MC) ICP and Agilent 7900 triple quadrupole QQQ ICP. The Nu-Plasma2 was set up to
22 collect U and all Pb isotopes were measured using high sensitivity ion counters. The Agilent
23 quadrupole was set up to collect the following trace elements, each of which were monitored for
24 0.03 s: ^{29}Si , ^{31}P , ^{49}Ti , ^{89}Y , ^{90}Zr , ^{93}Nb , ^{147}Sm , ^{151}Eu , ^{157}Gd , ^{159}Tb , ^{163}Dy , ^{165}Ho , ^{166}Er , ^{168}Tm ,
25 ^{172}Yb , ^{175}Lu , ^{178}Hf , ^{204}Pb , ^{232}Th , ^{238}U . Analyses are performed on a single isotopic peak, but
26 calibrated against a concentration standard to reflect the total elemental concentration. Analyses
27 were performed with a laser repetition rate of 6 Hz using a 23 μm spot diameter at 26%
28 attenuation, resulting in a power output of $\sim 2 \text{ J/cm}^2$ at the sample surface. A single analysis
29 involved two cleaning pulses, an initial background collection of 30 s, followed by 25 s of
30 ablation, and 15 s of washout time. Laser gas flows of 320 ml/min He, and 1.2 ml/min N were
31 used, with matched mass spectrometer argon gas flows of $\sim 1 \text{ ml/min}$ on the Nu Plasma2 and ~ 1
32 l/min on the Agilent. Limits of detection (LODs) are calculated using the “normal” method
33 within the Iolite software, and are reported in the Supplementary data table. All elements of
34 interested plotted in the main figures are above LOD with respect to their uncertainties.

35 The time-resolved mass spectra were reduced using the U_Pb_Geochronology4 data
36 reduction scheme in Iolite (Paton et al., 2011). The primary reference material used in this study
37 was OG1 (3465 Ma \pm 0.6 Ma; (Stern et al., 2009) with 91500 (1062.4 \pm 0.4 Ma; (Wiedenbeck et
38 al., 1995), Plešovice (337.1 \pm 0.4 Ma; (Sláma et al., 2008), GJ1 –(601.9 \pm 0.7 Ma; (Jackson et al.,
39 2004) and Curtin University internal standard KLDF (552.9 \pm 0.3 Ma) used as secondary age
40 standards. $^{206}\text{Pb}/^{238}\text{U}$ ages calculated for the secondary zircon age standards were used to
41 calculate an additional uncertainty required for a single analytical population in these materials.
42 This additional uncertainty of \sim 1% was incorporated into the calculation of the $^{206}\text{Pb}/^{238}\text{U}$ age of
43 the unknown analyses. For the calculation of other weighted means and the plotting of concordia
44 diagrams an additional 0.5% uncertainty was added to the analytical uncertainties for the
45 $^{207}\text{Pb}/^{235}\text{U}$ and $^{207}\text{Pb}/^{206}\text{Pb}$ ratios. Internal standardization for trace elements used a Zr
46 concentration of 43.14 wt% in zircon standard GJ-1 (Jackson et al., 2004). All analyses were
47 monitored for common Pb using measured ^{204}Pb on the quadrapole relative to standard
48 reference materials that are free of common b. All reported analyses fall within the zero common
49 Pb baseline determined by such standards.

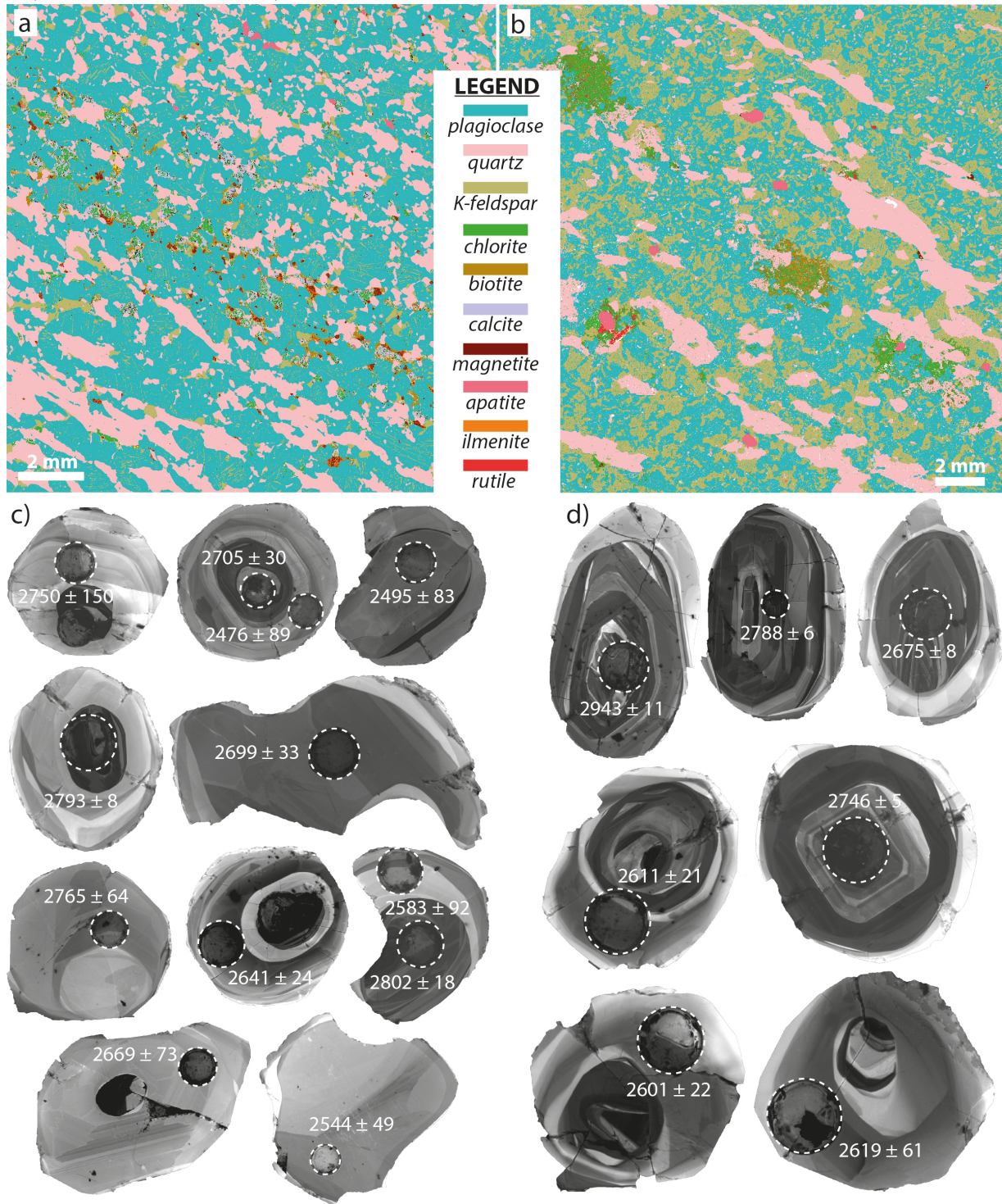
50 **1.2 Scanning electron microscopy**

51 Cathodoluminescence images were acquired using a Quanta 650F, Field Emission Gun (FEG)
52 Scanning Electron Microscope (SEM) at the University of Cambridge. Imaging used a 7 kV
53 beam current and a working distance of 11.5 mm. QEMSCAN (Quantitative Elemental Mapping
54 SCANning) images were obtained using the same Quanta 650F, Field Emission Gun (FEG)
55 Scanning Electron Microscope (SEM), equipped with two Bruker XFlash 6130 Energy
56 Dispersive Spectrometers (EDS) at the Department of Earth Sciences, University of Cambridge,
57 which includes an automated spectrum acquisition and classification procedure. Analyses were

58 performed by obtaining field-scans, providing a complete characterisation of particle surfaces
59 above a predefined electron backscatter threshold. The brightness coefficients were calibrated
60 against quartz, gold and copper. Spectra were collected at 25 kV and 10 nA with 2000 total X-
61 ray counts at a 10µm spacing, and compared to a Species Identification Protocol (SIP) that
62 discriminate minerals on the basis of their characteristic X- ray and electron backscatter
63 intensities.

64

65 **2 SAMPLE DESCRIPTIONS**



66

67 Supp Figure 1. Qemscan automated mineral analysis maps of thin sections for samples a)

68 NWS17/6 and b) NWS17/7 in this study, showing mineral sizes and proportions. Representative

69 CL images of zircon grains for samples a) NWS17/6 and b) NWS17/7 in this study, showing
70 locations of LASS analysis and associated Pb–Pb ages.

71

72

73 **2.1 Tonalitic gneiss (sample NWS17/6)**

74 Sample NWS17/6 is a coarse-grained grey felsic igneous rock in which the quartz crystals have a
75 lilac tinge characteristic of granulite facies metamorphism. A weak foliation is defined by quartz
76 ribbons and more mafic bands, although irregular centimetre-scale patches of mafic minerals
77 also occur. Based on QEMSCAN thin section analysis (Figure 2a), the sample is dominated by
78 plagioclase (57%) and quartz (31%) with grain sizes typically ranging from 200µm to ~2mm ,
79 with subordinate K-feldspar (6%), the latter occurring both as interstitial grains and as exsolved
80 lamellae within plagioclase (antiperthite) and chlorite (2%). Bands of mafic minerals display a
81 smaller grain size up to ~300–400µm. Minor (<1%) minerals include calcite, biotite, magnetite,
82 hematite, ilmenite, pyrite, apatite and zircon grains with rounded ‘soccer ball’ morphologies.

83 **2.2 Monzogranite (sample NWS17/7)**

84 Sample NWS17/7 is a foliated pink felsic igneous rock. The QEMSCAN analysis (Figure 2b)
85 shows the rock is dominated by plagioclase (44%) and K-feldspar (29%) up to ~1mm in size,
86 and coarser-grained quartz (19%) that commonly forms ribbons up to 10mm in length that define
87 the foliation. Large irregular aggregates of biotite and chlorite (up to 5mm) help define the
88 foliation in hand sample, and are associated with fine-grained rutile and epidote. Accessory
89 minerals include coarse apatite, magnetite, rutile and subrounded ‘soccer ball’ grains of zircon.

90

91 **3 RESULTS**

92 **3.1 Zircon textures**

93 Typical CL images of zircon textures are provided in Figure 2c (NWS17/6) and Figure 2d
94 (NWS17/7). Spot locations for LA–MC–ICP–MS analyses are marked in the images, along with
95 the corresponding $^{207}\text{Pb}/^{206}\text{Pb}$ spot ages and associated 2σ analytical uncertainties. A small
96 number of analyses overlap core/rim zones. The bottom of laser pits show a characteristic CL
97 pattern and are used as part of the criteria for the inclusion or exclusion of some analyses. All
98 analyses used a laser diameter of 30 μm that can be used as a scale bar for individual zircon
99 grains.

100 **3.1.1 Tonalitic gneiss (sample NWS17/6)**

101 Grain sizes for zircons are typically 100–300 μm with CL images indicating a range of internal
102 textures. A number of grains show a darker CL central portion that commonly preserve faint
103 oscillatory zoning. In all cases this region shows evidence of ‘bleaching’ (Hoskin and Black,
104 2000), whereby the zoning is more diffuse or irregular in places. This is suggestive that all
105 portions of the grain underwent high temperature recrystallisation. Many grains have a bright CL
106 rim up to ~ 100 μm in width that shows a variety of zoning patterns. Some rims exhibit broad but
107 irregular oscillatory zoning, whereas others contain irregular patches of varying CL response. A
108 few grains show distinct sector and ‘fir tree’ zoning patterns. Some grains show no apparent core
109 region, although this may be a cut effect.

110 **3.1.2 Monzogranite (sample NWS17/7)**

111 The grain size of zircon grains in this sample are similar to those within the tonalitic gneiss, but
112 there are more grains with an elongate or ‘rugby ball’ morphology, with aspect ratios $\sim 2:1$. Most

113 grains show a darker CL core region that exhibits a variety of textures from fine-scale oscillatory
114 zoning to features suggesting recrystallization (Hoskin and Black, 2000; Taylor et al., 2016).
115 Most grains have a distinctive rim up to $\sim 50 \mu\text{m}$ in width that has irregular curvilinear internal
116 features that truncate zoning patterns within the core. These zones may exhibit vague oscillatory
117 zoning, show sector zoning, or preserve a combination of the two.

118

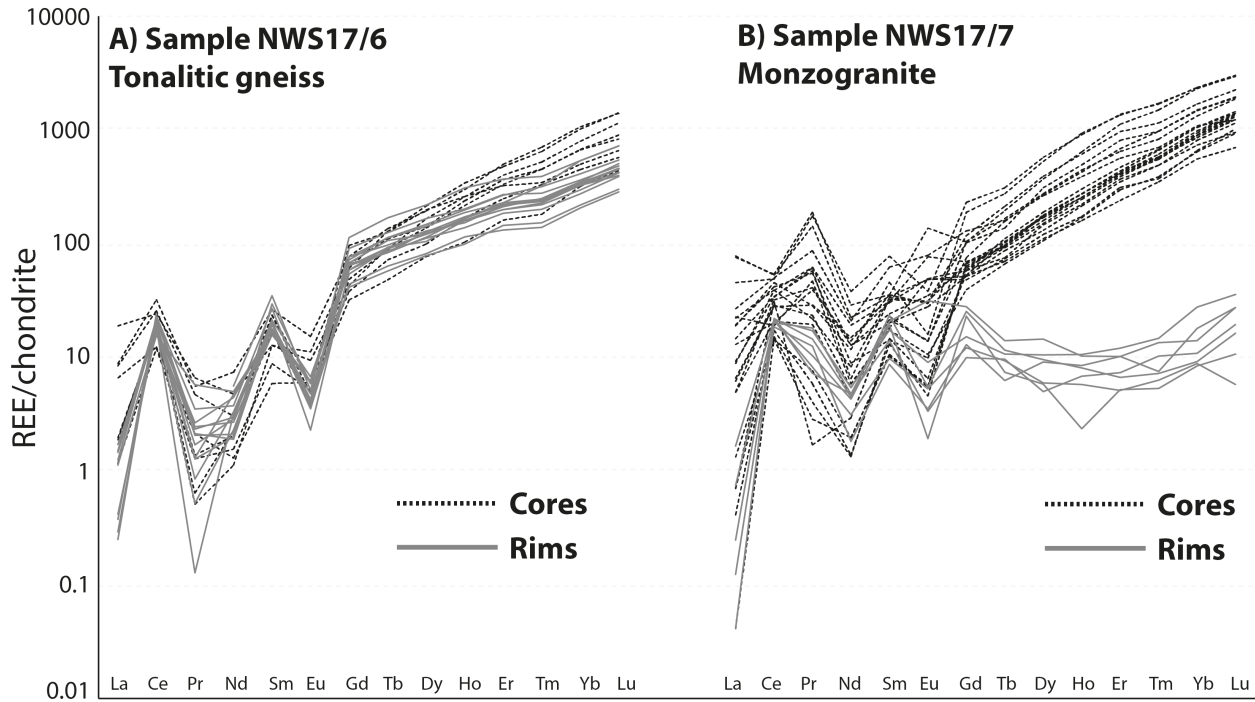
119 **3.2 Zircon trace element geochemistry**

120 Due to a lack of any clear correlation between age and the CL texture of zircon grains, trace
121 element variations have simply been displayed as a function of age regardless of CL textural type
122 in Supplementary Figure 1. Tonalitic gneiss analyses are displayed related to the 3 time periods
123 identified in the main text and main Figure 4, monzogranite analyses are displayed as cores and
124 distinct rims.

125 **3.2.1 Tonalitic gneiss (sample NWS17/6)**

126 Trace element variations highlight three distinct time periods in the tonalitic gneiss: analyses
127 older than *c.* 2680 Ma (Group 1), analyses between *c.* 2680 Ma and *c.* 2550 Ma (Group 2 - grey
128 field in Supplementary Figure 1), and analyses younger than *c.* 2550 Ma (Group 3). Group 1
129 (2802–2699 Ma) is generally the most distinctive. Some trace element characteristics (e.g. Hf/Y
130 and total REE) indicate a distinct compositional change at the onset of growth of Group 2 zircon
131 (2669–2583 Ma) (Figure 4). In a few cases, e.g. for Nb/Yb, Group 3 analyses (2544–2476 Ma)
132 are compositionally distinct from Group 2, suggesting new geological conditions. Some values
133 and ratios, in particular Th/U and Ti that are among the most commonly analysed trace elements,
134 are not particularly diagnostic, which may have hampered interpretation in previous studies.

135 Supplementary Figure 1a shows that Group 1 analyses predominantly have Hf/Y ratios <35
136 whereas groups 2 and 3 have Hf/Y > 35, with a small increase towards the younger end of Group
137 2 to a maximum of 66. Th/U ratios do not clearly discriminate between any of the groups
138 (Supplementary Figure 1b), nor do Ti concentrations that range from 11 to 14 ppm
139 (Supplementary Figure 1c). Total rare earth element (REE) contents fall from 213–395 ppm in
140 Group 1 (one outlier), to <200 ppm in groups 2 and 3, with a minimum ~120 ppm at the younger
141 end of Group 2 (Supplementary Figure 1d). Supplementary Figure 1e shows the fluctuation in
142 Nb/Yb ratios, for which Group 1 zircon grains have values of 0.007–0.009, Group 2 show
143 elevated values of 0.012–0.014, and Group 3 range more widely from 0.006 to 0.012
144 (Supplementary Figure 1e). Variations in U/Yb ratio do not correlate with age group, and scatter
145 between 0.1 and 1.6 (Supplementary Figure 1f). Group 1 zircon grains show Ce/Yb ratios of
146 0.07–0.17, whereas groups 2 and 3 are mostly higher (0.21–0.35 with one outlier; Supplementary
147 Figure 1g). The middle to heavy REE slope (Supplementary Figure 2a) is scattered for Group 1
148 zircon ($Yb_N/Gd_N = 5-17$; Supplementary Figure 1h), whereas groups 2 and 3 show a small shift
149 to lower values (4–6 with one outlier; Figure 6h).



150

151 3.2.2 Monzogranite (sample NWS17/7)

152 Zircon grains from this sample show a more dramatic variation in trace element concentrations,
 153 for which the *c.* 2605 Ma rim analyses have distinctive compositions. In almost all cases, cores
 154 with ages between *c.* 2800 and *c.* 2680 Ma (i.e. matching Group 1 from the tonalitic gneiss) have
 155 trace element characteristics that are indistinguishable from the tonalitic gneiss. The only
 156 exception is Ti concentrations, which are higher in the monzogranite (18–33 ppm;
 157 Supplementary Figure 1c). Hf/Yb ratios for core analyses are 14–51, whereas rim analyses range
 158 from 555 to 2760. Variations in Th/U are more distinctive than in the tonalite—cores range from
 159 0.2 to 1.2, whereas rim analyses are higher (1.4–3.3; Supplementary Figure 1b). Measured Ti
 160 concentrations are on average higher than the tonalite but shows some scatter, in which cores
 161 have 10–42 ppm Ti and rims have 14–26 ppm (Supplementary Figure 1c). Total REE
 162 concentrations are 206–551 for the core analyses, but are significantly lower for rim analyses
 163 (22–37; Supplementary Figure 1d). Ratios of Nb/Yb within the cores are 0.003–0.017, whereas

164 rims have higher and more scattered values (0.066–1.37; Supplementary Figure 1e). Similar
165 results are obtained for U/Yb (cores = 0.4–3; rims = 11–108), and Ce/Yb (cores = 0.1–0.2; rims
166 = 3–20) ratios (Supplementary Figure 1f,g). Values of Yb_N/Gd_N (Supplementary Figure 1h and
167 Supplementary Figure 2b), shows consistent values in zircon cores (8–19), whereas rims values
168 are relatively, and distinctly, depleted ($Yb_N/Gd_N = 0.4–1.9$).

169

170 9 REFERENCES

- 171 Hoskin, P.W.O., Black, L.P., 2000. Metamorphic zircon formation by solid-state recrystallization of
172 protolith igneous zircon. *Journal of Metamorphic Geology*, 18(4): 423-439.
- 173 Jackson, S.E., Pearson, N.J., Griffin, W.L., Belousova, E.A., 2004. The application of laser ablation-
174 inductively coupled plasma-mass spectrometry to in situ U-Pb zircon geochronology.
175 *Chemical Geology*, 211(1-2): 47-69.
- 176 Kylander-Clark, A.R.C., Hacker, B.R., Cottle, J.M., 2013. Laser-ablation split-stream ICP
177 petrochronology. *Chemical Geology*, 345: 99-112.
- 178 Paton, C., Hellstrom, J., Paul, B., Woodhead, J., Hergt, J., 2011. Iolite: Freeware for the visualisation
179 and processing of mass spectrometric data. *Journal of Analytical Atomic Spectrometry*,
180 26(12): 2508-2518.
- 181 Sláma, J. et al., 2008. Plešovice zircon - A new natural reference material for U-Pb and Hf isotopic
182 microanalysis. *Chemical Geology*, 249(1-2): 1-35.
- 183 Stern, R.A., Bodorkos, S., Kamo, S.L., Hickman, A.H., Corfu, F., 2009. Measurement of SIMS
184 instrumental mass fractionation of Pb isotopes during zircon dating. *Geostandards and*
185 *Geoanalytical Research*, 33(2): 145-168.
- 186 Taylor, R.J., Kirkland, C.L., Clark, C., 2016. Accessories after the facts: Constraining the timing,
187 duration and conditions of high-temperature metamorphic processes. *Lithos*, 264: 239-257.
- 188 Wiedenbeck, M. et al., 1995. Three natural zircon standards for U-Th-Pb, Lu-Hf trace element and
189 REE analyses. *Geostandards Newsletter*, 19: 1-24.

190

191